AIAA Aviation Forum and ASCEND co-located Conference Proceedings
21 - 25 July 2025, Las Vegas, Nevada
AIAA AVIATION FORUM AND ASCEND 2025

10.2514/6.2025-3158

Design of a Micro-Compressor for Deflected Slipstream CoFlow Jet Airfoils in Martian Conditions

Yan Ren * Gecheng Zha †
CoFlow Jet, LLC.
http://coflowjet.com
4649 Ponce de Leon Blvd, Suite 306, Coral Gables
FL 33146, USA
yren@coflowjet.com

1 Abstract

This study presents the design and analysis of a micro-compressor system tailored for ultra-low air density conditions, specifically to match the Martian atmosphere. The micro-compressor is a critical component for the Deflected Slipstream CoFlow Jet (DS-CFJ) airfoil aircraft, intended to enable sustained vertical takeoff/landing flight in the conditions of Mars. The Martian atmosphere, with its extremely low density, poses significant challenges for generating sufficient lift and maintaining efficient propulsion. The micro-compressor is designed to enhance the performance of the DS-CFJ system by providing the necessary airflow to increase lift and remove flow separation, with a design target of a total pressure ratio ($P_{tr} = 1.6$) and a mass flow rate of 2.9 g/s, thus enabling efficient aerodynamic performance. The micro-compressor performance is based on the requirement of the MAGGIE (Mars Aerial and Ground Global Intelligent Explorer) aircraft design.

Using computational fluid dynamics (CFD) simulations, the micro-compressor is designed for minimal power consumption while achieving the target total pressure ratio and mass flow rate under Martian conditions. The results demonstrate that the micro-compressor can obtain the requirements of the MAGGIE CFJ electric VTOL aircraft. This research lays the foundation for future development of Martian aircraft, highlighting the potential of integrating micro-compressor technology with CFJ airfoils to overcome the limitations posed by the low-density Martian environment.

2 Deflected Slipstream VTOL

The deflected slipstream (DS) concept pioneered by Kuhn and Draper in the late 1950's [1–3] generates hover lift by deflecting the slipstream from the propeller downward using a deflected flap. Once airborne, the flap is retracted for high-speed cruise. A 90° deflected slipstream would turn a full horizontal propeller thrust to a vertical lift. However, flow suffers severe separation when the flap angle is large. A double-plain flap system tested was able to deflect the flow by 45° [1]. A double-slotted flap [2] increased the deflection to 63°. Such a flow deflection is not sufficient for hover, in particular with the ground effect. The efforts using DS for VTOL were abandoned in 1960's. Antcliff et al at NASA [4] recently revisited the DS concept and suggested using CoFlow Jet (CFJ) flow control to enhance the flow turning. They envision that the deflected slipstream eVTOL as the second generation UAM vehicles "could provide benefits in cruise efficiency, weight, noise, reliability, and maintainability, and offer safer transition characteristics" [4].

* CoFlow Jet, LLC., CTO, Ph.D., AIAA member
† CoFlow Jet, LLC., President, AIAA Associate Fellow, Professor of the University of Miami

2.1 Deflected Slipstream Enabled by CoFlow Jet

CFJ is a zero-net-mass-flux (ZNMF) active flow control technique recently developed by Zha and his team [5–12, 12–17]. As illustrated in Fig. 1, a small amount of mass flow is drawn into the airfoil near the trailing edge, pressurized and energized by a micro-compressor system inside the airfoil, and then injected near the leading edge in the direction tangent to the main flow. CFJ achieves ultra-high lift coefficient exceeding the theoretical limit [16], thrust generation, and very high stall angle of attack (e.g., 70°) with low energy expenditure.

Fig. 2 is the photo of the CFJ-NACA6421 airfoil recently tested in wind tunnel with 5 compressors embedded inside the airfoil along the span [18]. A C_{Lmax} of 8.6 is achieved, far greater than 1.5 of the baseline airfoil [18]. The CFJ airfoil also generates very high thrust up to $C_D = -1.0$. The operating range of CFJ airfoil without stall is dramatically increased. The CFJ airfoil has very low energy expenditure, which is the unique feature enabling CFJ wing to obtain very high productivity efficiency at cruise when the flow is benign at low angle of attack [14, 19–21].

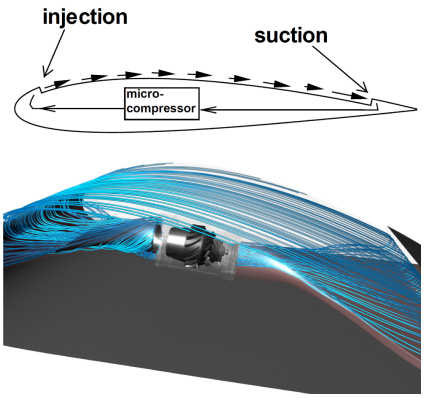

Figure 1: CFJ airfoil concept and micro-compressor embedded.

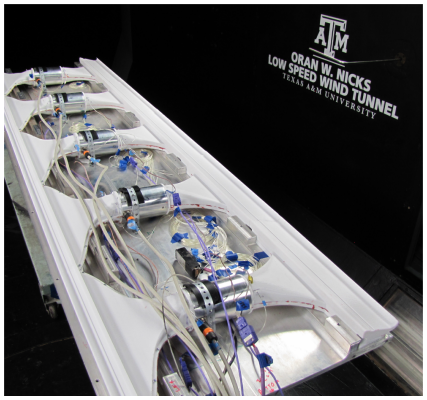

Figure 2: Photo of the wind tunnel tested airfoil with 5 compressors embedded.

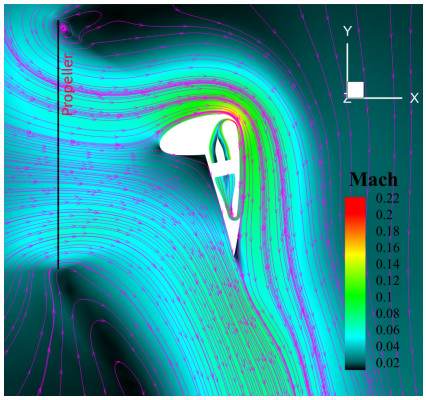

Figure 3: 3D CFD simulated DS-CFJ airfoil at static hover conditions.

Fig. 3 is the mid-section of CFD result for the 3D DS-CFJ wing with the micro-compressor (Fig. 1) embedded in the single plain flap in Earth conditions. It shows that the slipstream from the propeller is deflected 88° by the CFJ flap at static hover condition. Single plain flaps will have the lowest mechanical complexity basically the same as conventional takeoff/landing (CTOL) aircraft, much lower than the titling wings or articulating propellers. The ground effect can be eliminated if the wing is 2.3D above the ground (D: prop. diameter) or the propeller is slightly mounted upward as shown in Fig. 4 with the wing 1.5D above the ground. The slipstream is turned 90°, hits the ground and bifurcates to flow upstream and downstream. The DS-CFJ airfoil concept is demonstrated in testing conducted in a static condition [22]. Fig. 5 shows the 2D cruise flow of the DS-CFJ airfoil with the flap retracted at Mach 0.15. It has C_L=1.4, C_L/C_D=107.8, $C_L/(C_D + P_c)$ =74 (P_c: CFJ power coefficient), and C_μ=0.03. CFJ appears to be the only active flow control that could achieve extraordinary cruise efficiency due to its low energy expenditure [12, 14, 19, 23, 24]. Conventional airfoil with C_L=1.4 would be nearly stalled with a large drag and poor C_L/C_D. CFJ appears to be the only active flow control that can benefit the entire flight envelop at high lift takeoff/landing and cruise conditions.

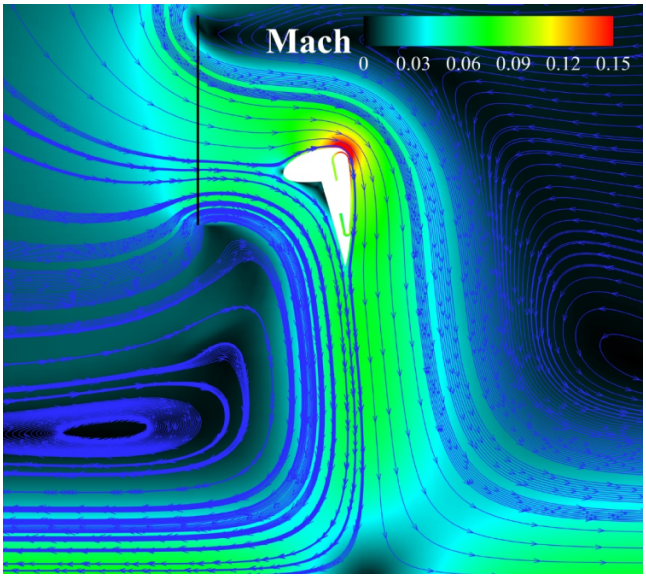

Figure 4: Hover with ground effect.

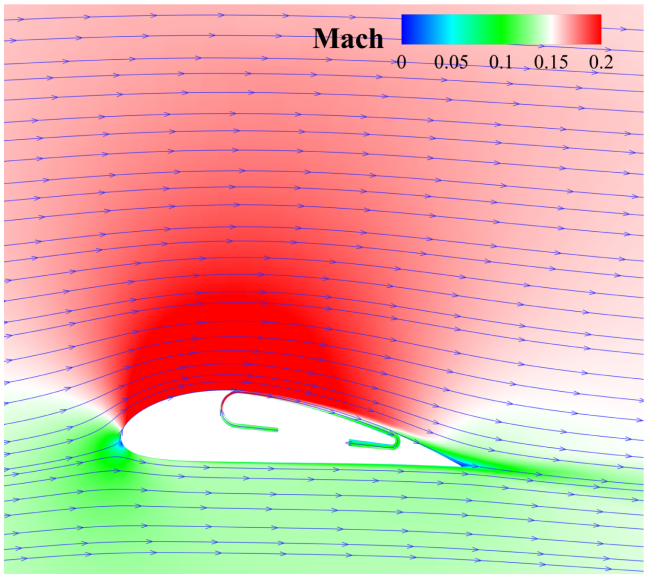

Figure 5: DS-CFJ airfoil at high efficiency cruise.

The CFD simulation of the DS-CFJ airfoil above is conducted using our in house high order CFD code, FASIP (Flow-Acoustics-Structure Interaction Package) developed under various government agencies(AFOSR, NASA, ARO, NSF, GUIde) [9, 12, 14, 15, 25–48]. FASIP has high order WENO schemes (5th and 7th) [26–34,49] for the inviscid fluxes and fully conservative 4th and 6th order central differencing schemes for the viscous fluxes [26, 27]. It incorporates advanced turbulence modeling with RANS, IDDES, and LES. The CFD simulation and FASIP code are intensively validated with CFJ experiment for aerodynamic forces and power consumption [9, 12, 16, 17, 35, 36, 45, 46, 48].

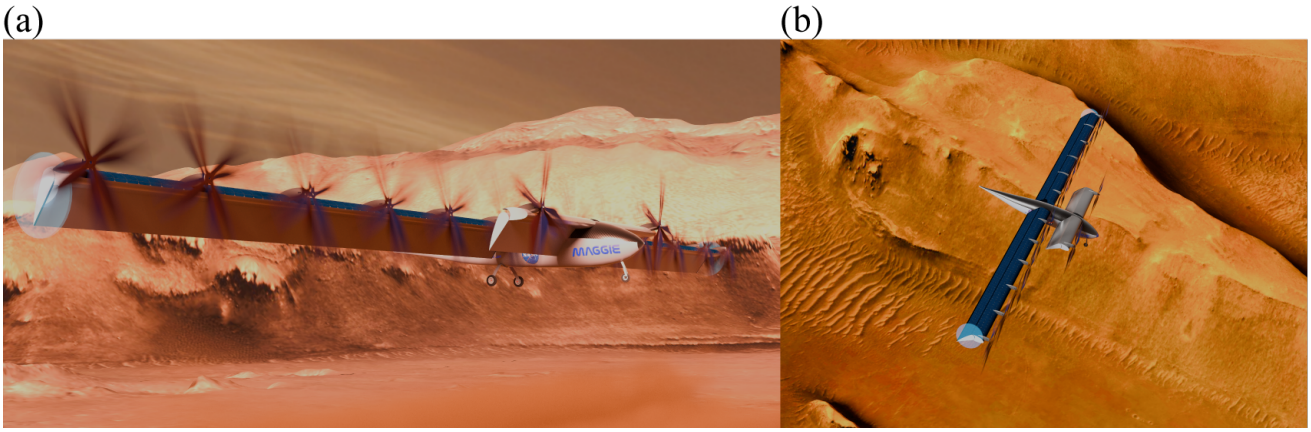

Figure 6: (a) DS-eVTOL at hover with the plain CFJ flap down and (b) cruise with the flap retracted.

2.2 Mars Aerial and Ground Global Intelligent Explorer (MAGGIE)

Recently, MAGGIE aircraft concept is studied for Mars science exploration missions. MAGGIE is a solar powered electric VTOL aircraft that is able to cover the entire Martian surface in a year. Due to DS-CFJ, MAGGIE does not need to use tiltrotors, tiltwings, or lift-plus-cruise configurations. Fig. 6 shows the MAGGIE configuration at hover and cruise. For Mars, the battery-powered micro-compressors are sized for the planet's thin CO_2 atmosphere. These compressors supply the airflow, and the CFJ mechanism needs to achieve high lift at hover and to high lift coefficient with excellent aerodynamic efficiency at cruise. The purpose of this paper is to conduct the preliminary design and

analysis to demonstrate the feasibility of the micro-compressors to satisfy the CFJ requirements in the Martian atmosphere with very low density mostly consisting of carbon dioxide.

3 Results

This section documents the aerodynamic and performance characteristics of the axial micro-compressor in three steps. First, the overall annulus and meridional geometry are introduced (Fig. 7) and key dimensions and operating targets are listed in Table 1; span-wise thickness and camber trends that accommodate ultra-low Reynolds numbers are then quantified in Fig. 8. Second, blade-resolved CFD at the design point visualises the three-dimensional flow field (Fig. 9) and span-wise streamlines (Fig. 10), confirming that the passage flow remains fully attached from hub to tip. Finally, compressor maps covering five rotational speeds (Fig. 11) demonstrate that the unit reaches the target mass flow of $2.9\,\mathrm{g\,s^{-1}}$ and pressure ratio of $P_{t,r} = 1.6$ with a broad operation range of the blade height and peak isentropic efficiency near the design point. Together, these results verify that the geometry, flow behavior, and performance envelope meet the stringent requirements of Martian operation.

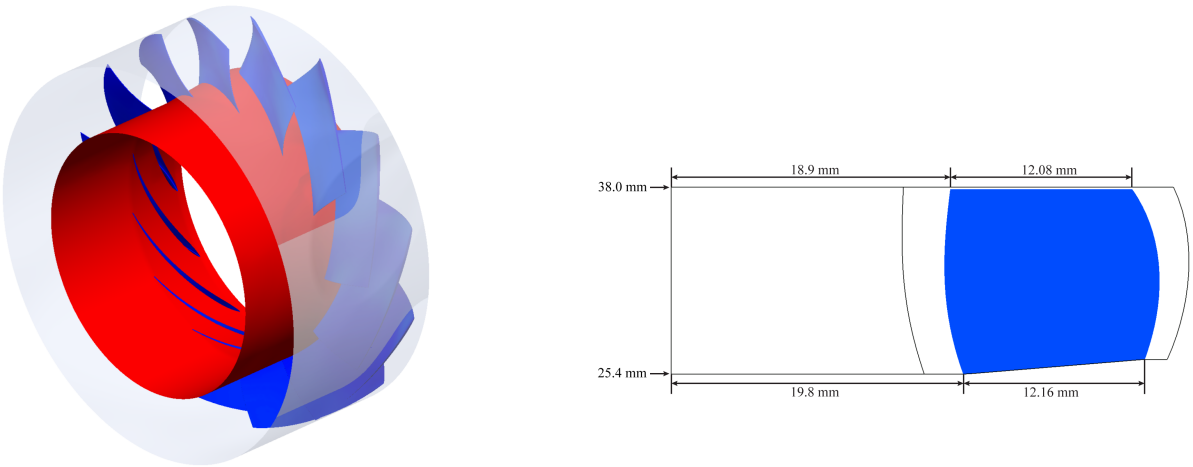

(a) (b)

Figure 7: (a) Full annulus of the compressor model, and (b) meridional view.

3.1 Compressor geometry

Figure 7(a) shows the complete annulus of the compressor model, while Figure 7(b) presents its meridional section. Table 1 details the geometric and operational parameters, including a nodal diameter of 15, a hub radius of 25.4 mm, and a casing radius of 38 mm. The compressor is designed to operate at 85 000 RPM with a mass flow rate of 2.9 g/s, a total pressure ratio of 1.6. These specifications form the basis for a comprehensive aerodynamic and thermodynamic analysis, evaluating the compressor's viability for sustained operation in the low-density Martian atmosphere.

Figure 8 presents the compressor blade thickness and mean line angle β distributions as functions of the meridional distance (M) for five radial spans: 0.0, 0.25, 0.5, 0.75, and 1.0. In Figure 8(a), the blade thickness increases from the leading edge to approximately two-thirds of the chord length, then tapers toward the trailing edge. The outer spans (e.g., 1.0) exhibit a lower peak thickness compared to the hub region (0.0). Meanwhile, Figure 8(b) shows that the β angle steadily increases with M, indicating a progressive change in blade curvature from the leading edge to trailing edge. These variations in thickness and angle across the span highlight how the blade geometry is tailored to accommodate different flow conditions at various radial locations.

Table 1: Compressor Geometry and Operating Parameters

Nodal diameter	15
Hub radius	25.4 mm
Casing radius	38.0 mm
Rotational speed	85,000 RPM
Design mass flow rate	2.9 g/s
Design total pressure ratio	1.6
Tip clearance	1.2%

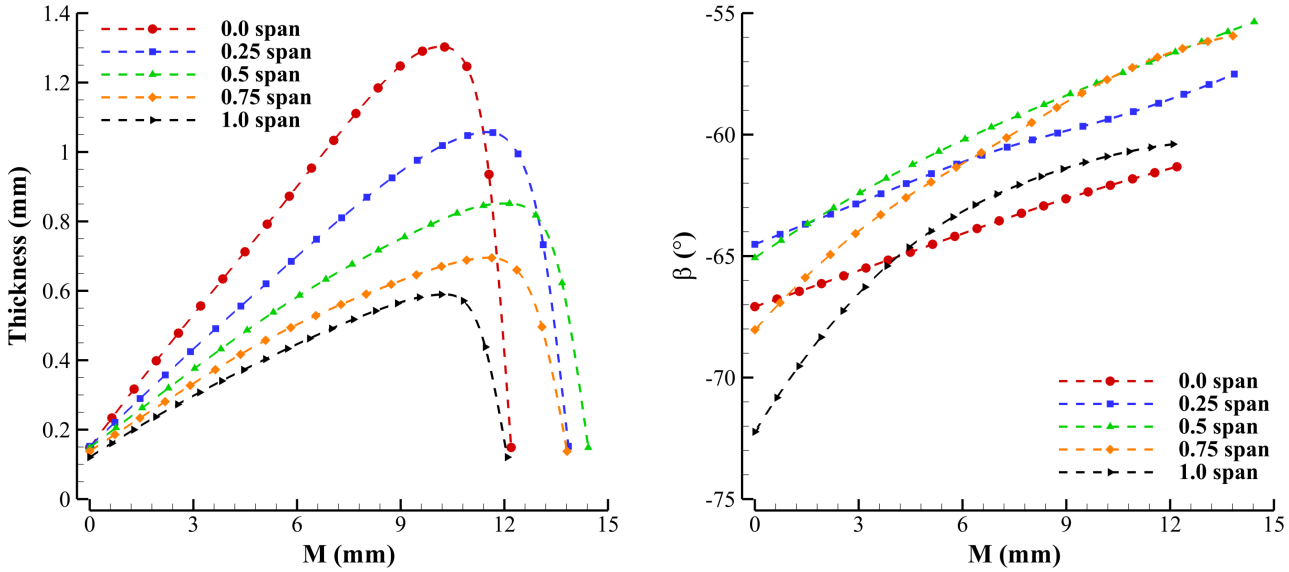

(a) (b)

Figure 8: Compressor blade geometric parameters: (a) blade thickness; (b) β angle.

3.2 Compressor flow field at the design point

Figure 9 provides a comprehensive view of the flow field within the compressor. In Figure 9(a), the full annulus visualization with streamlines highlights the overall flow structure, showing how the working fluid accelerates and turns through the blade passages. Figures 9(b)–(d) illustrate the Mach number distribution at three spanwise locations (0.1, 0.5, and 0.9), capturing the progressive variation in flow speed and blade loading from near the hub to near the tip. Regions of high Mach numbers, indicative of elevated local flow velocities, can be observed at mid to outer spans, reflecting the influence of blade geometry and increasing radius on flow acceleration. These visualizations collectively demonstrate how the flow evolves from the inlet to the outlet, helping to identify key areas of potential aerodynamic loss or flow separation.

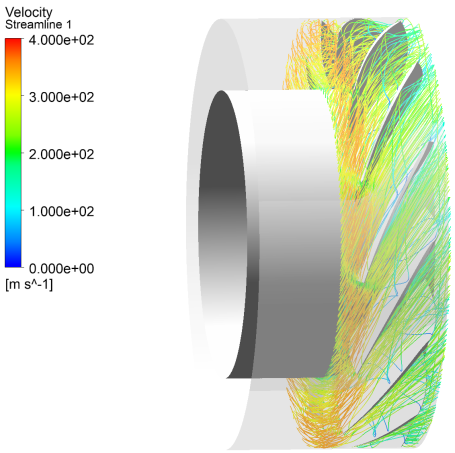

(a) Full annulus with streamlines

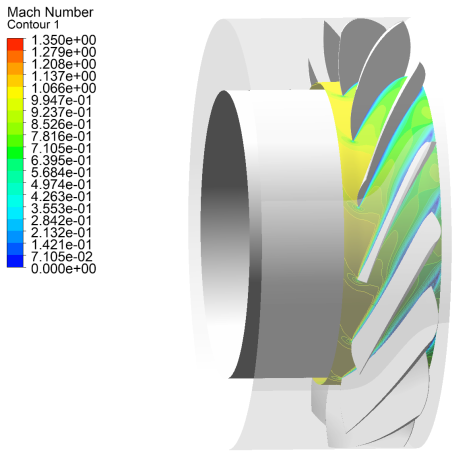

(b) Mach contour at span = 0.1

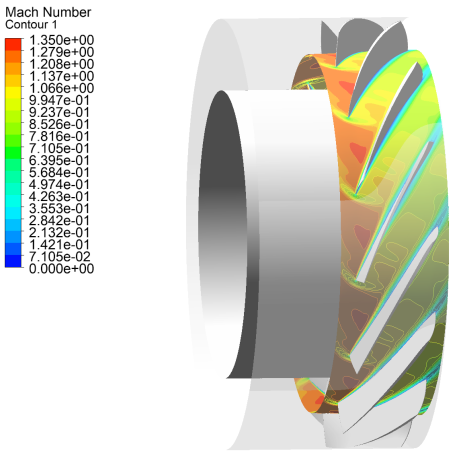

(c) Mach contour at span = 0.5

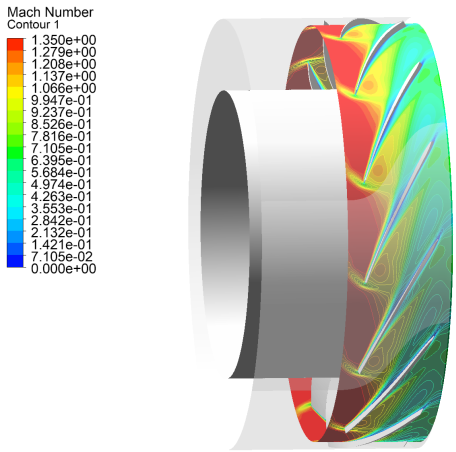

(d) Mach contour at span = 0.9

Figure 9: Flow field comparison along the annulus: (a) full annulus with streamlines; (b) Mach contour at span = 0.1; (c) Mach contour at span = 0.5; and (d) Mach contour at span = 0.9.

Figure 10 illustrates the flow streamlines at three radial spans (0.1, 0.5, and 0.9) within the compressor, each colored by local relative flow velocity. Near the hub region (span = 0.1), the streamlines reveal relatively moderate flow speeds and a clear path along the blade surfaces, indicating the absence of flow separation. By mid-span (span = 0.5), the flow accelerates, as shown by the higher velocity range, and still maintains attached flow. Closer to the tip (span = 0.9), the flow speeds are generally higher, reflecting the combined influence of larger tangential velocities and blade curvature. Throughout the entire span, no evidence of separation is observed, suggesting that the blade design effectively manages flow from hub to tip.

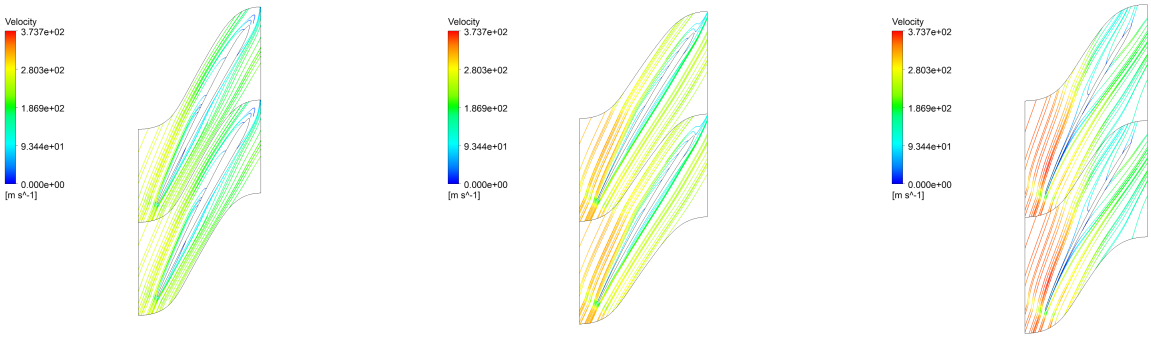

(a) Streamlines at span = 0.1 (b) Streamlines at span = 0.5 (c) Streamlines at span = 0.9

Figure 10: Comparison of streamlines at different spanwise positions. Colored by flow velocity.

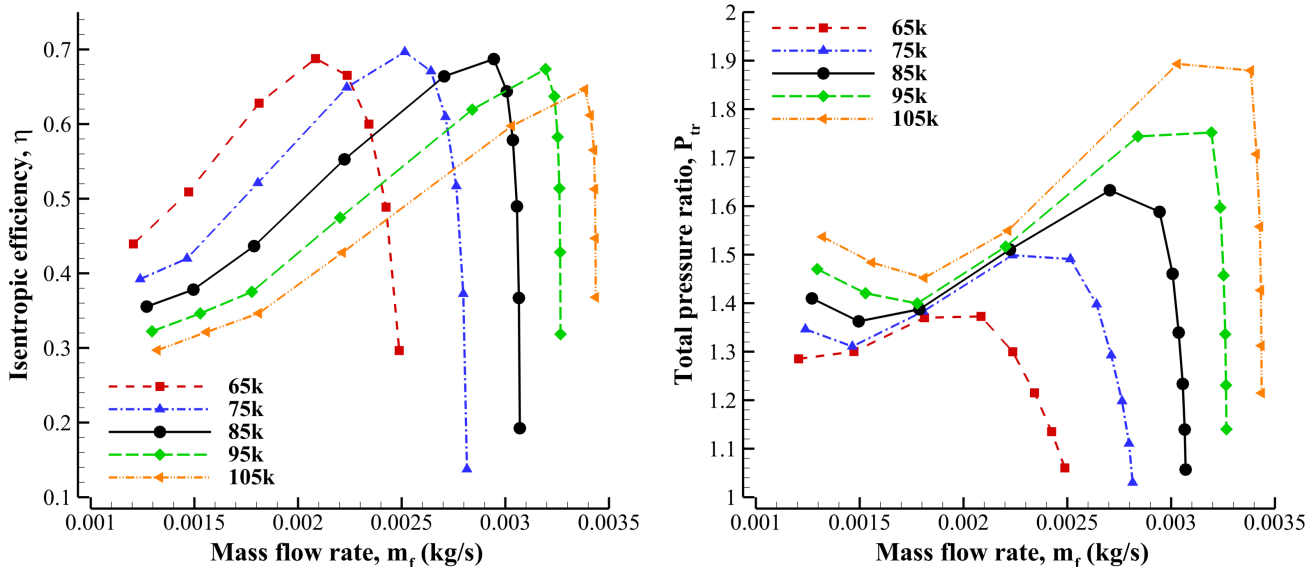

(a) Isentropic efficiency vs. mass flow rate (b) Total pressure ratio vs. mass flow rate

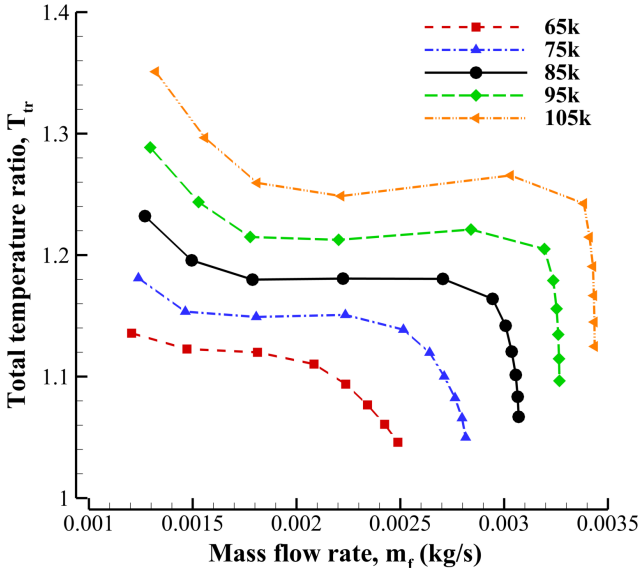

(c) Total temperature ratio vs. mass flow rate

Figure 11: Compressor maps showing performance parameters as functions of mass flow rate.

3.3 Compressor map

Figure 11 illustrates the performance maps of the compressor at five different rotational speeds, highlighting variations in isentropic efficiency, total pressure ratio, and total temperature ratio as functions of mass flow rate. In Figure 11(a), the design speed of 85 k RPM (black curve) reaches its highest efficiency near $\dot{m} = 0.0029\,\mathrm{kg/s}$, marking the design point. This operating condition strikes a balance between aerodynamic loading and flow capacity, remaining safely clear of the stall/surge limit at lower flows and the choke boundary at higher flows.

Figure 11(b) shows that the total pressure ratio rises with speed and attains a peak at intermediate flow rates, moving to far left at the stall condition and right at the choked condition on each speed line reduces the pressure-raising capability. Additionally, this compressor demonstrates a wide operating range, spanning total pressure ratios from about 1.3 up to 1.9, with relatively high isentropic efficiency. In Figure 11(c), the total temperature ratio reflects the increasing work input at higher speeds, with the highest values corresponding to the 105 k RPM curve. Overall, the maps indicate robust performance and operational flexibility, allowing for efficient operation at various flow rates without encountering significant stall or choke issues within a wide operating range.

4 Conclusions

A single-stage, battery-powered axial micro-compressor is designed and numerically simulated to operate in Mars's atmospheric conditions with mostly CO2 at $p_\infty \approx 600\,\mathrm{Pa}$, $T_\infty \approx 240\,\mathrm{K}$. The 85 000-RPM unit—hub radius 25.4 mm, tip radius 38 mm—meets the target mass flow of $2.9\,\mathrm{g\,s^{-1}}$ and total-pressure ratio $P_{t,r} = 1.6$. Blade-resolved CFD shows fully attached flow from hub to shroud, with span-wise thickness and camber distributions optimised for Reynolds numbers two orders of magnitude below terrestrial practice. Performance maps reveal a broad operating range (pressure ratios 1.3–1.9) and peak isentropic efficiency 70% at the design point. These results confirm that a compact, ultra-low-Re axial compressor can reliably provide the pressure ratio and mass flow required for CFJ active flow-control applications under Martian conditions, paving the way for hardware fabrication and experimental testing. Future work will include design optimization of the spanwise loading to further improve the rotor efficiency , OGV design for stage performance, and structural analysis to ensure the structure integrity.

5 Acknowledgment

This project is sponsored by NASA NIAC Grant Number 80NSSC24K0647. The numerical simulation is conducted with the computing resource of NASA High-End Computing systems. We greatly appreciate all the support from NASA.

References

[1] R. E. Kuhn and J. W. Draper, "An Investigation of a Wing-Propeller configuration Employing Large-Chord Plain Flaps and Large-Diameter Propellers for Low-Speed Flight and Vertical Take-Off ." NACA TN-3307, December 1954.

[2] R. E. Kuhn and J. W. Draper, "Investigation of Effectiveness of Large-Chord Slotted Flaps in Deflecting Propeller Slipstreams Downward for Vertical Take-Off and Low-Speed Flight ." NACA TN-3364, Jan. 1955.

[3] R. E. Kuhn, "Investigation of the Effects of Ground Proximity and Propeller Position on the Effectiveness of a Wing with Large-Chord Slotted Flaps in Redirecting Propeller Slipstreams Downward for Vertical Take-Off ." NACA TN-3629, March 1956.

[4] K. R. Antcliff, S. K. Whireside, L. W. Kohlman, and C. Silva, "Baseline Assumptions and Future Research Areas for Urban Air Mobility Vehicles." AIAA Paper 2019-0528, AIAA SciTech 2019 Forum, San Diego, CA, 7-11 January 2019.

[5] Zha, G.-C. and Gao, W. and Paxton, C., "Jet Effects on Co-Flow Jet Airfoil Performance," *AIAA Journal, No. 6,*, vol. 45, pp. 1222–1231, 2007.

[6] G.-C. Zha and D. C. Paxton, "A Novel Flow Control Method for Airfoil Performance Enhancement Using Co-Flow Jet." *Applications of Circulation Control Technologies*, Chapter 10, p. 293-314, Vol. 214, Progress in Astronautics and Aeronautics, AIAA Book Series, Editors: Joslin, R. D. and Jones, G.S., 2006.

[7] Zha, G.-C and Paxton, C. and Conley, A. and Wells, A. and Carroll, B., "Effect of Injection Slot Size on High Performance Co-Flow Jet Airfoil," *AIAA Journal of Aircraft*, vol. 43, 2006.

[8] Zha, G.-C and Carroll, B. and Paxton, C. and Conley, A. and Wells, A., "High Performance Airfoil with Co-Flow Jet Flow Control," *AIAA Journal*, vol. 45, 2007.

[9] Wang, B.-Y. and Haddoukessouni, B. and Levy, J. and Zha, G.-C., "Numerical Investigations of Injection Slot Size Effect on the Performance of Co-Flow Jet Airfoil ," *AIAA Journal of Aircraft*, vol. 45, pp. 2084–2091, 2008.

[10] B. P. E. Dano, D. Kirk, and G.-C. Zha, "Experimental Investigation of Jet Mixing Mechanism of Co- Flow Jet Airfoil." AIAA-2010-4421, (5th AIAA Flow Control Conference, Chicago, IL), 28 Jun - 1 Jul 2010.

[11] B. P. E. Dano, G.-C. Zha, and M. Castillo, "Experimental Study of Co-Flow Jet Airfoil Performance Enhancement Using Micro Discreet Jets." AIAA Paper 2011-0941, 49th AIAA Aerospace Sciences Meeting, Orlando, FL,, 4-7 January 2011.

[12] Lefebvre, A. and Dano, B. and Bartow, W. and Di Franzo, M. and Zha, G.-C., "Performance and Energy Expenditure of Co-Flow Jet Airfoil with Variation of Mach Number," *AIAA Journal of Aircraft*, vol. 53, pp. 1757–1767, 2016.

[13] Lefebvre, A. and Zha, G.-C., "Numerical Simulation of Pitching Airfoil Performance Enhancement Using Co-Flow Jet Flow Control." AIAA Paper 2013-2517, AIAA Applied Aerodynamics Conference, San Diego, CA, 24 - 27 June 2013.

[14] Lefebvre, A. and Zha, G.-C. , "Design of High Wing Loading Compact Electric Airplane Utilizing Co-Flow Jet Flow Control." AIAA Paper 2015-0772, AIAA SciTech2015: 53rd Aerospace Sciences Meeting, Kissimmee, FL, 5-9 Jan 2015.

[15] Liu, Z.-X. and Zha, G.-C., "Transonic Airfoil Performance Enhancement Using Co-Flow Jet Active Flow Control." AIAA Paper 2016-3472, AIAA AVIATION 2016, 8th AIAA Flow Control Conference, Washington, D.C, June 13-17, 2016.

[16] Yang, Y.-C. and Zha, G.-C., "Super-Lift Coefficient of Active Flow Control Airfoil: What Is the Limit?." AIAA Paper 2017-1693, AIAA SCITECH2017, 55th AIAA Aerospace Science Meeting, Grapevine, Texas, 9-13 January 2017.

[17] K.-W. Xu and G.-C. Zha, "High control authority 3d aircraft control surfaces using co-flow jet," *AIAA Journal of Aircraft*, July 2020.

[18] G.-C. Zha, Y.-C. Yang, Y. Ren, and B. McBreen, "Super-lift and thrusting airfoil of coflow jet-actuated by micro-compressors." AIAA Paper 2018-3061, AIAA AVIATION 2018, Atlanta, GA , 25 - 29 June 2018.

[19] Y. Wang and G.-C. Zha, "Study of 3D Co-flow Jet Wing Induced Drag and Power Consumption at Cruise Conditions." AIAA Paper 2019-0034, AIAA SciTech 2019, San Diego, CA, January 7-11, 2019.

[20] Y. Wang, Y.-C. Yang, and G.-C. Zha, "Study of Super-Lift Coefficient of Co-Flow Jet Airfoil and Its Power Consumption." AIAA Paper 2019-3652, AIAA Aviation 2019, AIAA Applied Aerodynamics Conference, Dallas, Texas, 17-21 June 2019.

[21] Yang, Y.-C. and Zha, G.-C., "Numerical Investigation of Performance Improvement of the Co-Flow Jet Electric Airplane." AIAA Paper 2018-4208, AIAA AVIATION Forum 2018, 2018 Applied Aerodynamics Conference, Atlanta, Georgia, June 25-29, 2018.

[22] G. Zha, Y. Ren, W. Fredericks, and S. Whiteside, "Design and testing of deflected slipstream airfoil for vtol hover enabled by coflow jet," in *AIAA AVIATION FORUM AND ASCEND 2024*, p. 4420, 2024.

[23] Y. Wang and G.-C. Zha, "Study of Mach Number Effect for 2D Co-Flow Jet Airfoil at Cruise Conditions." AIAA Paper 2019-3169, AIAA Aviation 2019, AIAA Applied Aerodynamics Conference, Dallas, Texas, 17-21 June 2019.

[24] Y. Ren and G.-C. Zha, "Performance enhancement by tandem wings interaction of coflow jet aircraft." AIAA Paper 2021-1823, 2021 AIAA SciTech Virtual Forum, 11-15 January, 2021.

[25] X. Chen and G.-C. Zha, "Implicit Application of Non-Reflective Boundary Conditions for Navier-Stokes Equations in Generalized Coordinates," *International Journal for Numerical Methods in Fluids*, vol. 50, 2006.

[26] Shen, Y.-Q. and Zha, G.-C. and Chen, X.-Y., " High Order Conservative Differencing for Viscous Terms and the Application to Vortex-Induced Vibration Flows," *Journal of Computational Physics*, vol. 228(2), pp. 8283–8300, 2009.

[27] Y.-Q. Shen and G.-C. Zha, "Large Eddy Simulation Using a New Set of Sixth Order Schemes for Compressible Viscous Terms ," *Journal of Computational Physics*, vol. 229, pp. 8296–8312, 2010.

[28] Shen, Y.-Q. and Zha, G.-C. and Wang, B.-Y., " Improvement of Stability and Accuracy of Implicit WENO Scheme," *AIAA Journal*, vol. 47, No. 2, pp. 331–344, 2009.

[29] Shen, Y.-Q. and Zha, G.-C. , " Improvement of the WENO Scheme Smoothness Estimator," *International Journal for Numerical Methods in Fluids*, vol. 64, p. DOI:10.1002/fld.2186, 2010.

[30] Shen, Y.-Q. and Zha, G.-C., " Improved Seventh-Order WENO Scheme ." AIAA Paper 2010-1451, 48th AIAA Aerospace Sciences Meeting, Orlando, FL, Jan. 4-6, 2010.

[31] Y.-Q. Shen and G.-Z. Zha , "Generalized finite compact difference scheme for shock/complex flowfield interaction," *Journal of Computational Physics*, vol. doi:10.1016/j.jcp.2011.01.039, 2011.

[32] Shen, Y.-Q. and Zha, G.-C., " Low Diffusion E-CUSP Scheme with High Order WENO Scheme for Preconditioned Navier-Stokes Equations ," *Journal of Computer and Fluids*, vol. doi:10.1016/j.compfluid.2011.10.013,, 2011.

[33] Y.-Q. Shen and G.-C. Zha, "Improvement of weighted essentially non-oscillatory schemes near discontinuities," *Journal of Computer and Fluids*, vol. doi: http://dx.doi.org/10.1016/j.compfluid.2014.02.010, 2014.

[34] G.-C. Zha, Y. Shen, and B. Wang, "An improved low diffusion E-CUSP upwind scheme ," *Journal of Computer & Fluids*, vol. 48, pp. 214–220, 2011.

[35] B.-Y. Wang and G.-C. Zha, "A General Sub-Domain Boundary Mapping Procedure For Structured Grid CFD Parallel Computation," *AIAA Journal of Aerospace Computing, Information, and Communication*, vol. 5, No.11, pp. 2084–2091, 2008.

[36] Im, H.-S. and Zha, G.-C. and Dano, B. P. E., "Large Eddy Simulation of Coflow Jet Airfoil at High Angle of Attack," *Journal of Fluid Engineering*, vol. 136(2), p. 021101, 2014.

[37] Wang, B. Y and Zha, G.-C., "High Fidelity Simulation of Nonlinear Fluid-Structural Interaction with Transonic Airfoil Limit Cycle Oscillations," *Journal of Fluids and Structures*, vol. doi:10.1016/j.jfluidstructs.2010.02.003, 2010.

[38] K.-W. Xu and G.-C. Zha, "Mitigation of Serpentine Duct Flow Distortion Using CoFlow Jet Active Flow Control ." AIAA-2020-2954, AIAA Aviation 2020 Virtual Forum, 15-19 June, 2020.

[39] Y.-C. Yang, W. B. Bartow, G.-C. Zha, H.-Y. Xu, and J.-L. Wang, "Large eddy simulation of base drag reduction using jet boat tail passive flow control," *Journal of Computers and Fluids*, vol. 198, Feb. 2020.

[40] D. Espinal, H.-S. Im, and G.-C. Zha, "Full-annulus simulation of nonsynchronous blade vibration excitation of an axial compressor," *Journal of Turbomachinery*, vol. 140, pp. 031008–1, 2018.

[41] J.-Y. Gan, H.-S. Im, X.-C. Chen, G.-C. Zha, and C. L. Pasiliao, "Delayed detached eddy simulation of wing flutter boundary using high order schemes," *Journal of Fluids and Structures*, vol. 71, pp. 199–216, 2017.

[42] Im, H-S. and Zha, G-C., " Investigation of Flow Instability Mechanism Causing Compressor Rotor Blade Non-Synchronous Vibration ," *AIAA Journal*, vol. 52, pp. 2019–31, 2014.

[43] Im, H-S. and Zha, G-C., " Delayed Detached Eddy Simulation of Airfoil Stall Flows Using High Order Schemes ," *ASME Journal of Fluids Engineering*, p. DOI: 10.1115/1.4027813, 2014.

[44] X.-Y. Chen, G.-C. Zha, and M.-T. Yang, "Numerical Simulation of 3-D Wing Flutter with Fully Coupled Fluid-Structural Interaction," *Journal of Computers & Fluids*, vol. 36, No. 5, pp. 856–867, 2007.

[45] Gan, J.-Y. and Zha, G.-C., "Comparison of Drag Prediction Using RANS models and DDES for the DLR-F6 Configuration Using High Order Schemes." AIAA Paper 2016-0553, AIAA SCITECH2016, AIAA Aerospace Science Meeting, San Diego, CA, 4-8 January 2016.

[46] Wang, B. Y and Zha, G.-C., " Detached-Eddy Simulation of a Co-Flow Jet Airfoil at High Angle of Attack ," *AIAA Journal of Aircraft*, vol. 48, pp. 1495–1502, 2011.

[47] Im, H-S., Chen, X-Y and Zha, G-C., " Detached Eddy Simulation of Rotating Stall Inception for a Full Annulus Transonic Rotor ," *AIAA Journal of Propulsion and Power*, vol. 28, No. 4, pp. 782–798, 2012.

[48] K.-W. Xu, Y. Ren, and G.-C. Zha, "Separation control by coflow wall jet." Proceedings of AIAA Aviation 2021, Aug. 2-6, 2021, Submitted to AIAA Journal, 2-6 Aug. 2021.

[49] Y.-Q. Shen, G.-C. Zha, " A robust seventh-order WENO scheme and its applications." AIAA-2008-0757, 2008.